Draft version September 4, 2021
Typeset using LaTeX **twocolumn** style in AASTeX63

Cosmicflows-4

R. Brent Tully,[1] Ehsan Kourkchi,[1] Hélène M. Courtois,[2] Gagandeep S. Anand,[1] John P. Blakeslee,[3] Dillon Brout,[4] Thomas de Jaeger,[1] Cullan Howlett,[5] Joseph B. Jensen,[6] Luca Rizzi,[7] Khaled Said,[5] Daniel Scolnic,[8] and Benjamin E. Stahl[9]

[1] *Institute for Astronomy, University of Hawaii, 2680 Woodlawn Drive, Honolulu, HI 96822, USA*
[2] *University of Lyon, UCB Lyon 1, CNRS/IN2P3, IUF, IP2I Lyon, France*
[3] *NSF's NOIRLab, Tucson, AZ 85719*
[4] *USA*
[5] *School of Mathematics and Physics, The University of Queensland, Brisbane, QLD 4072, Australia.*
[6] *Utah Valley University, Orem, UT, USA*
[7] *W.M. Keck Observatory, 65-1120 Mamalahoa Highway, Kamuela, HI 96743, USA*
[8] *Duke University*
[9] *Department of Astronomy, University of California, CA 94720-3411, USA*

ABSTRACT

Blah, blah, blah

1. INTRODUCTION

Cosmicflows is a program to compile galaxy distances and parse observed velocities into components due to the expansion of the universe and residuals due to gravitational interactions. The fundamental interest is to derive inferences regarding the large scale structure of the universe from galaxy test particle peculiar motions. This fourth release of the program follows those of Tully et al. (2008, 2013, 2016).

Contributions to the *Cosmicflows* program have come from work within our collaboration and from the literature. We consider methodologies that have been tested and have physical bases that are reasonably well understood. It is as great a consideration, though, that there be large overlaps between contributions. A sample with distances to only a few objects cannot confidently be meshed within a common scale so is not very useful.

We derive distance in significant numbers mainly from six methodologies. By far, the largest quantitative contributions are given by the Fundamental Plane (FP) correlation between the luminosity, surface brightness, and central velocity dispersion of early-type galaxies (Dressler et al. 1987; Djorgovski & Davis 1987) and the luminosity-rotation rate relation for spiral galaxies (Tully & Fisher 1977) (TFR). The individual errors in these cases are substantial (20−25%) but the objects are widely dispersed, providing a dense network of distance information extending to $\sim 0.05c$.

Two other methods probe substantial distances with greater accuracy but their contributions remain small. Supernovae of type Ia (SNIa) (Phillips 1993) provide distances with accuracy $\sim$ 7% out to $\sim 0.1c$. Surface brightness fluctuations (SBF) monitoring the degree of resolution of the old stellar populations of elliptical galaxies (Tonry & Schneider 1988) can give distances with $\sim 5\%$ accuracy tor targets within $\sim 0.03c$.

While comparisons between these four methods can be set on a common relative scale, it remains to give them an absolute calibration. Two methods provide a bridge: those provided by the Cepheid period-luminosity relation (CPLR) (Leavitt & Pickering 1912) and the constancy of stellar luminosities at the tip of the red giant branch (TRGB) (Lee et al. 1993). These methods provide accurate distances ($\sim 5\%$) but are restricted to less than ~ 20 Mpc.

There has been considerable effort to establish the absolute scale of the CPLR and TRGB procedures through geometrically based observations. Parallax distances can be established to Cepheids within our own galaxy (Benedict et al. 2007) and parallax distances to RR Lyrae and horizontal branch stars can establish the TRGB scale (Rizzi et al. 2007). It is anticipated that observations with GAIA (Clementini et al. 2018; Mould et al. 2019) will provide robust direct Cepheid and TRGB calibrations in the near future. Meanwhile, important links to an absolute scale are provided by detached eclipsing binaries in the Large Magellanic Cloud (Pietrzyński et al. 2019) and the maser system in the nuclear region of the galaxy NGC 4258 (Reid et al. 2019).

The main contributions in the first edition of *Cosmicflows* (Tully et al. 2008) were based on the TFR with optical photometry obtained one at a time and analog neutral Hydrogen (HI) linewidths. The catalog contained distances to 1,791 galaxies constrained to the limit 3,000 km s^{-1}.

Cosmicflows-2 (Tully et al. 2013) was expanded to include a much larger volume, peaking in numbers at 5,000 km s^{-1} with a tail extending to $\sim 15,000$ km s^{-1}. Most of the contributions came from the TFR, with as a major revision the employ of a rigorous algorithm in the reduction of digital HI spectra (Courtois et al. 2009, 2011b). Likewise, the photometric analysis was more rigorously defined (Courtois et al. 2011a; Sorce et al. 2012). The catalog then grew to include 8,188 galaxies.

The major addition to *Cosmicflows-3* (Tully et al. 2016) were FP distance measures from the 6dFGSv survey (Springob et al. 2014). This sample is entirely confined to the celestial south and abruptly cuts of at 16,000 km s^{-1}. A secondary addition came from the TFR method with infrared photometry provided by the Spitzer Space Telescope (Sorce et al. 2014). *Cosmicflows-3* provided distances for 17,699 galaxies. Coverage within $\sim 8,000$ km s^{-1} was reasonably balanced around the sky but at 8,000 to 16,000 km s^{-1} it strongly favored the southern hemisphere. The infrared TFR contribution was confined to within $\sim 6,000$ km s^{-1} but notably extended coverage to low galactic latitudes, shrinking the coverage gap between galactic hemispheres.

Here with *Cosmicflows-4* a most important addition is a much extended TFR sample of 10,000 galaxies drawing in particular on kinematic information from ALFALFA, the Arecibo Legacy Fast ALFA survey of the high galactic latitude sky in the declination range $0 - 38$ degrees (Haynes et al. 2011, 2018). Photometry is provided by SDSS, the Sloan Digital Sky Survey (York et al. 2000) and WISE, the Wide-field Infrared Explorer (Wright et al. 2010). This component of *Cosmicflows-4* substantially redresses the imbalance favoring the southern sky of the previous catalog.

SDSS also provides the source material for a second even larger addition to the current catalog. SDSS photometry and spectroscopy are combined to provide FP distances to 30,000 galaxies out to 30,000 km s^{-1} in the quadrant of the sky that is celestial north and galactic north. In consequence, while *Cosmicflows-3* tilted toward coverage of the celestial south, now *Cosmicflows-4* greatly expands our knowledge of the north.

With the astronomical community's overriding interest in precision distance measurements in order to secure the value of the Hubble constant, there are understandable arguments for a maximally homogeneous approach (Riess et al. 2016). The *Cosmicflows* assembly is heterogeneous. It is to be appreciated that the primary interest of this program is the mapping of deviations from cosmic expansion, requiring coherence of distance measurements but not an absolute scaling. Nonetheless, the reasonable establishment of a zero point is not our most difficult task. Our heterogeneous approach has virtues. Results from separate methodologies can be compared by sectors of the sky or distance, potentially revealing systematics. Different contributions favor ancient populations or young, members of clusters or the field. Some are better probes of low galactic latitudes. Our samples are heterogeneous but not indiscriminate.

Coincidences of distance measurements by different methodologies to members of a common group enables the stitching of samples into a coherent ensemble. Our discussion will turn first to the important matter of the definition of groups in §2. Subsequent sections will give attention to each of the six methodologies that provide most of our distances. We begin with the numerically dominant TFR (§3) and FP (§4) components, benefiting from overlaps between large samples to establish coherence in a core compilation. We then give attention to the SBF (§5) and SNIa (§6) contributions that are modest in number but that impose demanding constraints. Mention will be made of a seventh method involving SNII that may hold promise for the future. This edifice is then be linked to foundational TRGB (§7) and CPLR (§8) information, these in turn grounded by geometrical maser[1] , eclipsing binary, and parallax observations.

2. GALAXY GROUPS

Galaxies tend to lie in groups, large and small. If associations are made correctly, then all distance measures to galaxies in a group should be the same within uncertainties. The composition of galaxy groups, then, is of major importance for our study for at least three reasons. First, averaging over the properties of a group reduces errors. With weighted averaging of distances, uncertainties can be brought down from single case 20-25% values (depending on the methodology) to statistical uncertainties of a few percent with some rich clusters. The gains apply to velocities as well. Velocity averaging can encompass *all* known group members, not just those with measured distances. Second, it is particularly important in the modeling of galaxy flows to accurately locate the rich clusters, where distance measures from at least the fundamental plane and surface brightness fluctuation targets congregate. Rich clusters tend to lie at focal points of galaxy streams.

Third, and perhaps most important, it is through the groups that we most effectively match the zero point scaling of the diverse samples. Given the potential for

[1] Studies of nuclear maser systems provide an eighth methodology and one that gives independent absolute distance estimates but these are only available for six galaxies. Discussed in §9.

systematics within samples, across sectors of the sky, and with distance, the more overlap the better. While there can be some overlap at the level of individual galaxies, by far most of our overlaps occur at the level of groups and clusters. A corollary benefit is the ability, in comparing distances to objects in common, to weed out egregiously bad data.

Galaxy groups come in a wide range of scales. We want to benefit from the advantages of grouping over the full range down to the instances of pairs. Typical friends-of-friends and related group algorithms do not scale physically over the three decades of mass of interest ($10^{12} - 10^{15}$ $M_\odot$). Appreciating the importance of the matter, we initiated studies resulting in three papers. In the first (Tully 2015a), we gave detailed attention to eight well-studied groups/clusters ranging from the Local Group to the Coma Cluster. It was possible in these eight clean cases to isolate an observable proxy for the virial radius of collapsed halos; the radius of second turnaround, R_{2t} (related to the "splashback" radius (Adhikari et al. 2014)). This radius is found to scale, as theory predicts, as $R_{2t} \propto M^{1/3}$ and $R_{2t} \propto \sigma_p$ for halos (groups, clusters) with mass M and velocity dispersion σ_p. This first paper establishes the coefficients of the scaling relationships.

In the second paper (Tully 2015b), the scaling relationships were applied to build a group catalog involving 43,000 galaxies in the 2MASS redshift survey essentially complete over the sky at $|b| > 5°$ for galaxies brighter than $K_s = 11.75$ (Huchra et al. 2012). The 2MASS survey gives good representation of the mass distribution within the volume extending to 15,000 km s^{-1} that concerns us, given its sensitivity to old stars. Relative distances are based on redshifts. We favor the use of this group catalog at systemic velocities greater than $\sim$ 3000 km s^{-1}. Were we to consider an alternative we would use the similarly physically motivated catalog by Lim et al. (2017).

Nearer than $\sim$ 3000 km s^{-1} confusion arising from peculiar velocities is severe and we have knowledge of a profusion of low surface brightness galaxies that fail to enter the 2MASS catalog. Hence, for the nearby volume we turn to the group catalog assembled in the third paper (Kourkchi & Tully 2017), based on a heterogeneous collection of all 15,000 galaxies with known velocities within 3,500 km s^{-1}. The groups are constituted based on the same scaling relations. The availability of distance information from *Cosmicflows-3* is tremendously helpful in resolving confusion issues and evaluating masses, hence scaling parameters.

With both the near and far catalogs, the groups are (roughly) bounded by the radius of second turnaround.

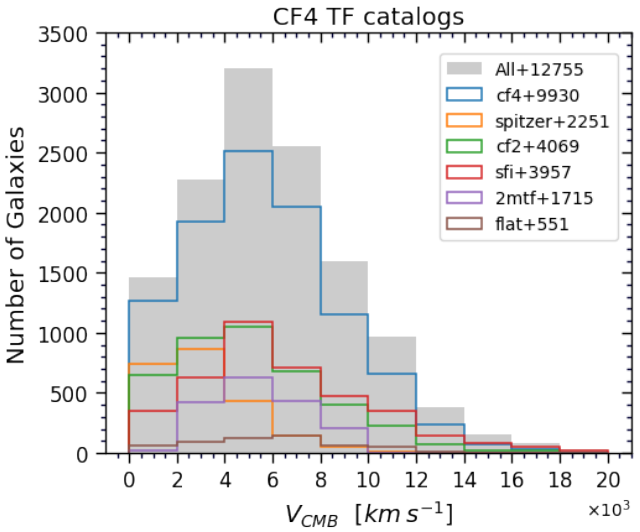

Figure 1. Cumulative histogram of TF targets with systemic velocity and a breakdown by sub-sample as given by the legend.

Hence they represent collapsed halos. As a naming convention, we identify a group by the Principal Galaxies Catalog number (Paturel et al. 1996) of the dominant member, which we call 1PGC. There can be inconsistencies between the two catalogs within 3,500 km s^{-1}. In such cases we favor the specifications by Kourkchi & Tully (2017).

These group catalogs provide an excellent description of clustering within $\sim 15,000$ km s^{-1}, the useful range of the 2MASS $K_s = 11.75$ redshift survey. However the SDSS based FP sample extends to $0.1c$. This SDSS FP sample is a sub-component of the Tempel et al. (2014) SDSS group catalog. If a group affiliation is unavailable for a galaxy within the groups described above then we opt for memberships in the Tempel et al. catalog.

3. LUMINOSITY-LINEWIDTH DISTANCES TO SPIRAL GALAXIES

Distances derived from the TFR are an extremely important component of the *Cosmicflows* program. They are numerous and the most widely distributed. Spiral galaxies are found in all environments, providing links with other methodologies in groups and sparse but invaluable coverage in voids.

Cosmicflows-4 assembles $\sim$ 12,500 TFR distances, the largest, most coherent compilation to date. The most important contribution (10,154 galaxies) is a new sample discussed by Kourkchi et al. (2019, 2020a,b) (Kourkch et al. 2021) (hereafter "cf4"). This new sample is compared and merged with five other TFR samples: the assembly of 5,980 cases in *Cosmicflows-2* that itself is broken into a part (4,069) derived within our col-

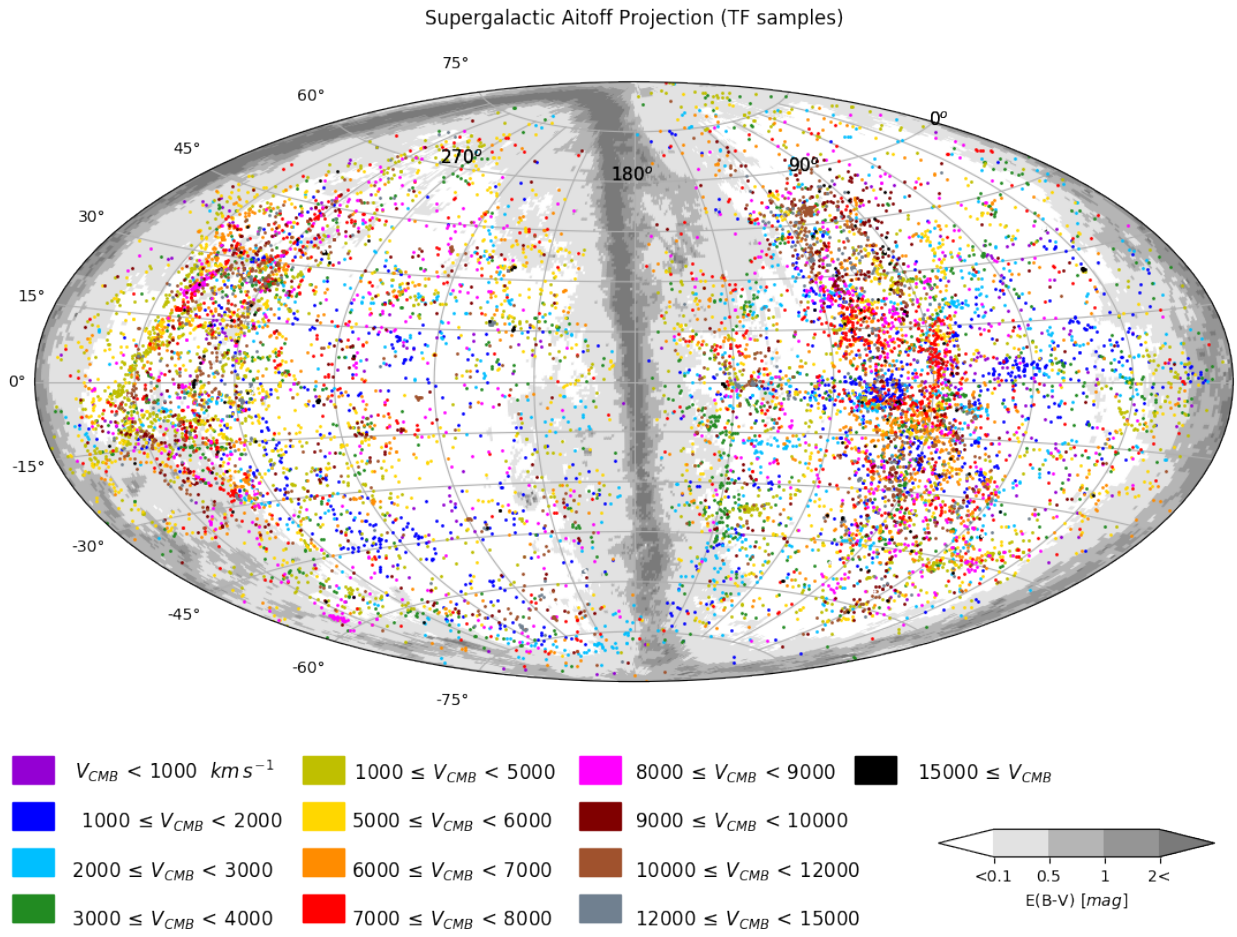

Figure 2. An Aitoff projection in supergalactic coordinates of the distribution of the ensemble of TF samples. Colors relate to systemic velocities of the group of a galaxy as given in the table below the map. Milky Way extinction levels are cast in shades of grey. The dense roughly vertical swaths of objects in both supergalactic hemispheres lie in the declination band of the Arecibo Telescope.

laboration (hereafter "cf2") and a part (3,957) emanating from the SFI++ study (Springob et al. 2007) (hereafter "sfi"), 2,251 galaxies discussed in *Cosmicflows-3* incorporating photometry from Spitzer Space Telescope images ("spitzer"), 1,715 galaxies utilizing 2MASS photometry ("2mtf") (Hong et al. 2019), and 551 extreme edge on galaxies (Makarov et al. 2018) ("flat").

Figure 1 is a histogram of the run of velocities for the TF sub-samples and the full TF sample. The distribution of the combined TF sample is displayed in supergalactic coordinates in Figure 2. The bands of high object density crossing the two supergalactic hemispheres lie in the $0 < \delta < 38$ declination zone accessed by Arecibo Telescope.

Our analysis began with each sample alone. At systemic velocities above $4,000$ km s^{-1} cosmic expansion velocities are expected to overwhelmingly dominate deviant velocities. Hence, a necessary (not sufficient) criterion a sample should satisfy is approximate constancy in the Hubble parameter for individual galaxies, V_i/d_i, averaged in velocity bins. The results of this test for all but the most recent flat galaxy sample were presented in Kourkchi et al. (2020b). A significant drift toward smaller $\langle H_i \rangle$ (larger derived distances) was evident in the "2mtf" sample. An adjustment to negate this trend was introduced by Kourkchi et al. (2020b), see §5, and is incorporated in the current work. The "flat" sample passes the $\langle H_i \rangle$ constancy test. Note that absolute $\langle H_i \rangle$ values are not an issue at this stage; they can be (and are) different for each sample.

This test of the constancy of H_i with redshift provides as a side product an evaluation of the *rms* dispersion in measurements within each sample. The measured values include dispersion in velocities and intrinsic dispersion but these components are unimportant if, as we do, we restrict attention to velocities greater than

4,000 km s^{-1}. We find the following characteristic *rms* dispersions for seven samples (treating separately the optical and infrared components of "cf4" (whence, "cf4-op" and "cf4-ir"), the two components of *Cosmicflows-2*, "cf2" and "sfi", and the components of "spitzer" with and without color corrections ("spitzer-cc" and "spitzer-nc"). From smallest to largest *rms* values: 0.37 for "cf4-op"; 0.39 for "cf4-ir"; 0.40 for all three "cf2", "sfi", and "spitzer-cc"; 0.50 for both "spitzer-nc" and "2mtf"; and 0.55 for "flat". Distance values for "2mtf" at local group frame velocities less than 2000 km s^{-1}, as evaluated by the Hubble parameter test and the test to be discussed next, are systematically too low and we reject all those "2mtf" measurements.

Another test of the samples applied by Kourkchi et al. (2020b) was to give attention to differences in distance moduli between "cf4" and the other sample: $\langle \mu_{cf4} - \mu_{alt} \rangle$ where *alt* is any of the other samples (now extended to include "flat"). This test is particularly useful for the isolation of egregiously bad distance values in one of the samples. Well less than 1% of cases in "cf2", "sfi", "spitzer", and "cf4" are rejected by this test. With "2mtf" $\sim 2\%$, and with "flat" $\sim 5\%$, are rejected.

We now give attention to the integration of these samples into a global maximally consistent compilation of TFR distances.

3.1. *Preliminaries*

Our goal is to combine the distinct TFR sub-samples into a single TFR sample. Before this integration, each sub-sample has its own zero point scaling. Here we revise the zero points of sub-samples to achieve statistical equality between them. We stress that we do not make relative changes in moduli *within* a sub-sample in this process. Doing so would subvert the utility provided by multiple sub-samples in reducing systematics.

It is evident that TFR samples have non-Gaussian outliers. Steps have been described to remove strongly deviant cases but our initial integration of sub-samples reveals additional instances. Applying a 3.5σ rejection criterion caught 275 cases among 22,233 measures (1.2%) where there would be 9 with a normal distribution. These outliers are removed.

Next, we want to profit from the advantages of averaging over groups discussed in §2. We begin by weighted averaging of the distance moduli of all galaxies within a 1PGC group within a single sub-sample. Individual weights are formed from the inverse square of *rms* uncertainties. This average and associated weight is one object in the ensuing analysis. Accordingly, each sub-sample is reduced to a quantity of objects (halos, groups, clusters) composed of from one to many individual galaxies, each identified by a 1PGC number.

3.2. *Combining all TFR distances: Bayesian approach*

Ultimately, we want to merge all samples by all methodologies into a coherent set with a zero point established by geometric distance measurements. At this stage, it is sufficient to bring all TFR sub-samples onto a common scale. The baseline TFR scale will be set by our new "cf4" sub-sample that should lie close to our final scale, given its linkage to Cepheid and TRGB measures as discussed by Kourkchi et al. (2020a,b).

Here, we pursue our goal to find the global modulus offset of each sample, "s", from that of "cf4", where "s" stands for any of the samples we introduced earlier in this chapter ("cf2", "sfi, "spitzer", "2mtf", "flat"). We will adjust the reported distance moduli of each sample, $DM_{in}^{(s)}$, following $DM^{(s)} = DM_{in}^{(s)} + \Delta\mu_s$ in order to set all cataloged distances on the same scale. By our convention, $\Delta\mu_{cf4} = 0$. We treat these adjusting values as a set of free parameters that are optimized together in a Bayesian framework. The best offset parameters minimize the total deviation of adjusted object distances (groups and individual galaxies) from the weighted distance averages offered by all samples together.

Our objective is to find the posterior probability distribution $\mathcal{P}(\Theta|\mathcal{D})$, with Θ being the vector of all moduli offsets, ($\Delta\mu_{s1}$, $\Delta\mu_{s2}$, ...). $\mathcal{D}$ holds the original cataloged distance moduli, $DM_{in}^{(s)}$. According to conditional probability theory, $\mathcal{P}(\Theta|\mathcal{D}) \propto \mathcal{P}(\mathcal{D}|\Theta)\mathcal{P}(\Theta)$. Having no prior knowledge about the distribution of the moduli offsets implies $\mathcal{P}(\Theta) = 1$ and subsequently $\mathcal{P}(\Theta|\mathcal{D}) \propto \mathcal{P}(\mathcal{D}|\Theta)$, where the right hand side is the likelihood function, $\mathcal{L}$. We assume that all measured object distances are independent with Gaussian uncertainties. Therefore, for each object, n, the likelihood function is the multiplication of a set of independent probabilities given as

$$\mathcal{L}_n = \prod_{All\ "s"} \frac{1}{\sqrt{2\pi\sigma_{n,s}^2}}\ \exp\frac{-1}{2}\Big(\frac{DM_n^{(s)} - \langle DM\rangle_n}{\sigma_{n,s}}\Big)^2\ , \tag{1}$$

iterating over all distance catalogs. $\langle DM\rangle_n$ is the weighted average distance of the n^{th} object that is derived from the adjusted distances, $DM_n^{(s)}$ is the distance modulus of the object in the sample "s", and $\sigma_{n,s}^2$ is the variance of $DM_n^{(s)} - \langle DM\rangle_n$, that is determined by adding the uncertainties of the associated parameters in quadrature. Likewise, the total likelihood function for all objects is $\mathcal{L}_{tot} = \prod_{n=1}^{N} \mathcal{L}_n$, where N is the total number of objects (groups and individuals). It is simpler to work with the logarithm of the likelihood function which

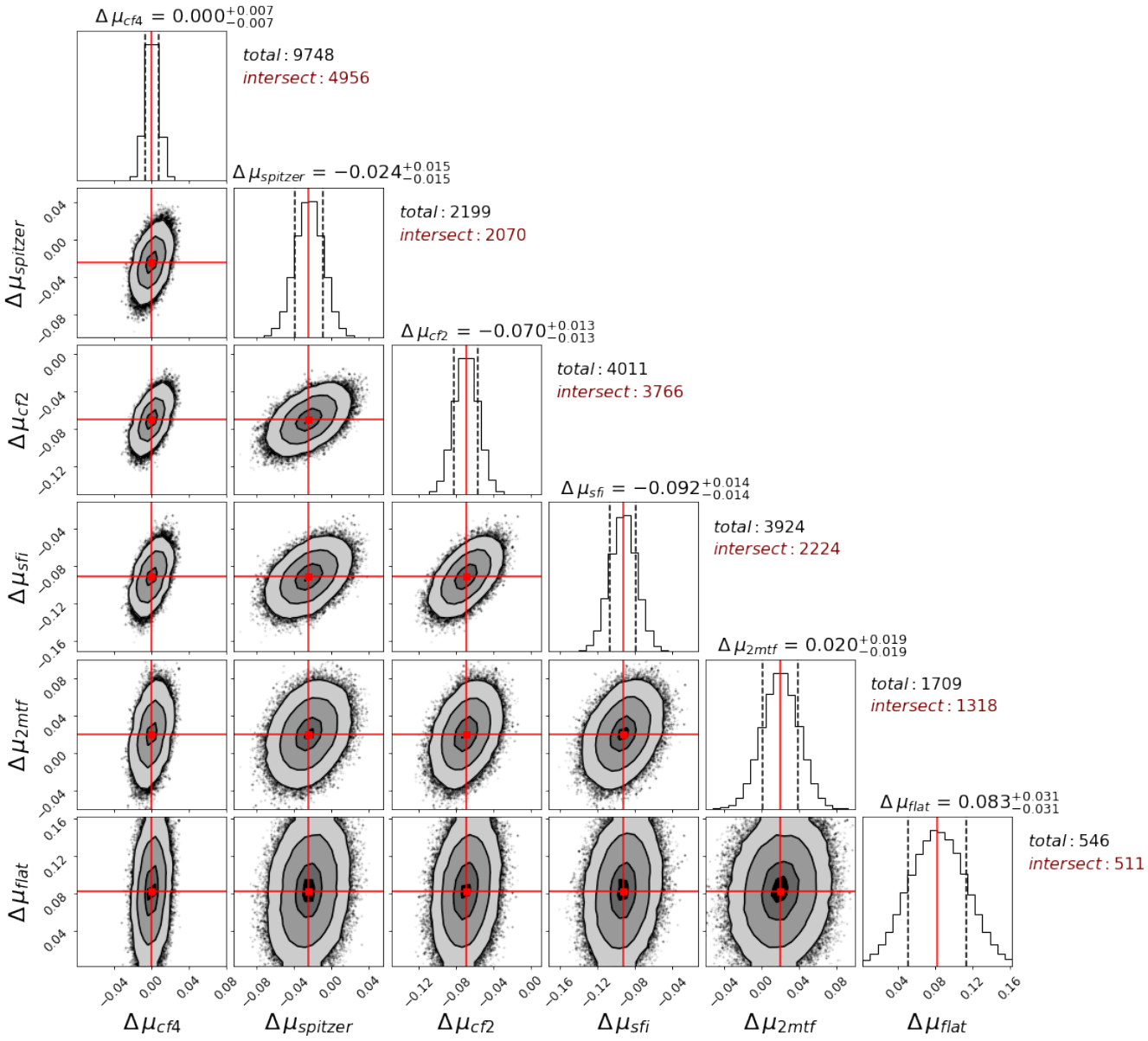

Figure 3. The posterior distribution of the optimized zero points of TFR catalogs with respect to "cf4". Contours represent $\sigma/2$, σ, $3\sigma/2$ and 2σ levels of the 2-dimensional distributions and they enclose 12%, 39%, 68% and 86% of the distributed points respectively. Two vertical dashed lines in each of the 1-dimensional histograms specify the region that accommodates 68% of the points, and the red vertical line identifies the median of the distribution. Each panel covers ±0.08 mag about the center of distribution.

is expressed as $\log\mathcal{L}_{tot} = -\sum_{n=1}^{N}\chi_n^2/2$, where

$$\chi_n^2 = \left(\frac{DM_n^{(s)} - \langle DM\rangle_n}{\sigma_{n,s}}\right)^2 . \qquad (2)$$

Adopting a flat prior distribution for the moduli offsets leaves us with a χ^2 minimization problem. We are interested in a set of moduli offsets that minimizes $\chi^2_{tot} = \sum_{n=1}^{N}\chi_n^2$.

To sample the posterior distribution, $\mathcal{P}(\Theta|\mathcal{D})$, we use the Python package *emcee* (Foreman-Mackey et al. 2013), that implements Markov Chain Monte Carlo (MCMC) simulations to explore the parameter space. Starting from our likelihood function, we generate 128 chains each with the length of 10,000. We remove the first 1,000 steps which is conservatively chosen to ensure that the remaining steps adhere to Markov chain statistics. Figure 3 illustrates the corner plots for the resulting posterior distribution of $\Delta\mu_s$. The top-most panel of each column shows the one dimensional distribution of the corresponding sampled parameter, overlaid with the median values (red solid line) and the lower/upper bounds corresponding to 16/84 percentiles

(black dashed line). Horizontal and vertical red lines in the 2-dimensional distributions exhibit the location of the median values that are adopted as the optimum moduli offsets of the corresponding catalogs with respect to "cf4".

The variance for a given sub-sample that is recorded in Fig. 3 depends on both the uncertainties in individual measurements and the number of intersections with other sub-samples. The individual uncertainties between the alternate TF sub-samples are only modestly different, so it is the numbers of intersections that dominate.

4. FUNDAMENTAL PLANE DISTANCES TO EARLY-TYPE GALAXIES

The Fundamental Plane (FP) methodology (Dressler et al. 1987; Djorgovski & Davis 1987), with its applicability to early-type galaxies, provides a complement to the TFR. The accuracies of individual measurements are comparable. While the gas-rich systems observed with the TFR are widely dispersed, the old star dominated systems favored for FP observations tend to clump in regions of high density.

Here in *Cosmicflows-4* we combine results from five programs. Three of these were already included in *Cosmicflows-2*: contributions for a total of 1508 galaxies to be referred to as "smac" (Hudson et al. 2001), "efar" (Colless et al. 2001), and "enear" (Bernardi et al. 2002). Individually these sources provide distances for 691, 696, and 449 galaxies, respectively. Contributions from a fourth program, 6dFGSv (Springob et al. 2014) were included in *Cosmicflows-3*. This sample of 8,885 galaxy distances is particularly important as the numerically dominant source of distances in the celestial south. However, by far the largest sample containing 30,152 galaxies is a new contribution restricted to the celestial and galactic north that draws on data extracted from the Sloan Digital Sky Survey (SDSS). The three earliest FP surveys, "smac", "efar", and "enear" provide valuable bridges across the celestial hemispheres.

4.1. *The 6dFGSv Sample*

While the 6dFGSv sample was originally included in *Cosmicflows-3*, in this latest work we provide a new recalibration of this sample based on the findings of Qin et al. (2018) designed to explore and remove spurious flows. In total, the 6dFGSv sample subtends the entire $\delta < 0°$ sky, except for regions with galactic latitute $|b| < 10°$. It's 8,885 objects encapsulate some of the brightest early-type galaxies in the 6-degree Field Galaxy Survey (6dFGS; Jones et al. 2009), nominally selected to have a spectral SNR > 5, total J-band magnitude < 13.65, redshift $cz < 16,500$km s^{-1} and velocity dispersion greater than 112km s^{-1} (Campbell et al. 2014). Further refinements to this selection include visual classification and removal of galaxies based on their morphological type (although as demonstrated in Tully et al. (2016) not all remaining galaxies are classified as ellipticals) and removal of objects with undesirable spectral features or poor spectral template fits (Campbell et al. 2014). Photometry for the Fundamental Plane sample was obtained by cross-matching with the 2MASS survey (Jarrett et al. 2000; Skrutskie et al. 2006).

With this sample, Springob et al. (2014) produce peculiar velocity measurements by modelling the (logarithmic) difference in observed and cosmological distances to each galaxy as a function of the (logarithmic) difference between their observed effective radii and the effective radii predicted from the best-fit Fundamental Plane. Simply put, for each galaxy one can compute the probability of it having a particular distance modulus by assuming a Gaussian probability distribution function (PDF) about the Fundamental Plane. However, this procedure is complicated by Malmquist bias and the selection function of the 6dFGSv data, particularly the magnitude limit. The presence of a magnitude limit cuts a slice through the Fundamental Plane, such that the PDF is no longer normalised. Because the magnitude limit is in apparent magnitudes, the portion of the Fundamental Plane that cannot be observed varies with distance, and so the normalisation of the PDF for each galaxy also depends on distance. To counteract this effect, Springob et al. (2014) produced a calculation of this normalisation as a function of distance using simulations drawn from the best-fit 6dFGSv Fundamental Plane with a $J < 13.65$ limit.

In subsequent work by Qin et al. (2018), similar simulations reproducing the Fundamental Plane, selection function and methodology applied to the 6dFGSv data were used to measure the bulk flow. A significant offset between the measured and true bulk flows in the simulations was identified in the direction directly toward the southern celestial pole. It was found possible to remove this effect in the simulations (and subsequently the data) by recalculating the normalisation of the probability distribution for each galaxy using an ad-hoc, brighter, magnitude limit of $J < 13.217$. In this work we repeat this calculation, paying special attention to not only the bulk flow, but also the Hubble parameter in radial shells.

We start by generating 128 mock 6dFGSv surveys matching the methods in Magoulas et al. (2012); Qin et al. (2019), which are then run through a reconstruction of the 6dFGSv pipeline using a magnitude limit of $J < 13.65$. Unlike previous works, the normalisation of

the PDF for each galaxy is computed using numerical Monte-Carlo integration of the truncated 3D Gaussian PDF, rather than summing over simulations. This procedure was found to result in less noise and was far more reliable for computing an accurate value at large comoving distances where by design the number of galaxies available to compute the probability, even over 128 simulations, quickly falls to zero.

The bulk flow in each simulation was then computed using the η-Maximum Likelihood Estimator (Kaiser 1988; Qin et al. 2018), as was the weighted mean value of

$$\log_{10}(H_i) = \log_{10}\left(\frac{V^i_{\rm mod}}{d_i}\right). \quad (3)$$

in redshift bins, where $V^i_{\rm mod} = cz_i(1 + 1/2[1 - q_0]z_i - 1/6[1 - q_0 - 3q_0^2 + j_0]z_i^2)$, z_i is the redshift of the galaxy, q_0 and j_0 are the acceleration and jerk parameters and c is the speed of light. Here, d_i is the luminosity distance to each galaxy, computed assuming $H_0 = 75$ km s^{-1} Mpc^{-1}. For comparison, the same quantities are computed for each simulation using the true luminosity distance and peculiar velocity of each simulated galaxy.

The results of this procedure are shown in Figs. 4 and 5. Also plotted alongside are the results for the original 6dFGSv data. From the binned Hubble parameters, it is clear that the mocks with distance moduli computed using the 6dFGSv pipeline exhibit an outflow and do not lie on the expected $H_0 = 75$ km s^{-1} Mpc^{-1} line. The distribution of these same mocks matches the data, which leads us to conclude the same is likely true for the data too. This trend is not obvious without the presence of simulations (and so not highlighted previously), particularly because cosmic variance at $cz_{\rm cmb} < 5000$ km s^{-1} seems to be scattering the observed Hubble parameters high in the data.

The effect on the bulk flow is particularly pronounced. It was found by Qin et al. (2018) that the measured bulk flow in the simulations is biased quite negatively in the direction of the southern celestial pole compared to the bulk flow known to exist in the simulations. Although the 'true' bulk flow in the 6dFGSv is not known and can only be estimated, the measured value is consistent with the biased mock results, leading us to conclude that the data is similarly biased.

As with the previous work by Qin et al. (2018), we correct for this problem by modifying the magnitude limit used in the Malmquist bias correction/normalisation of each galaxy's PDF. By iterating, a magnitude limit of $J < 13.38$ was found to produce binned Hubble parameters that are flat with redshift while also substantially reducing the difference between the adjusted and measured bulk flows. The results of applying this limit to the mocks and data are shown in Figs. 4 and 5. The small differences between the optimal value found here and that used in Qin et al. (2018) are likely the result of the more rigorous calculation of the normalisation using numerical integration adopted in this work.

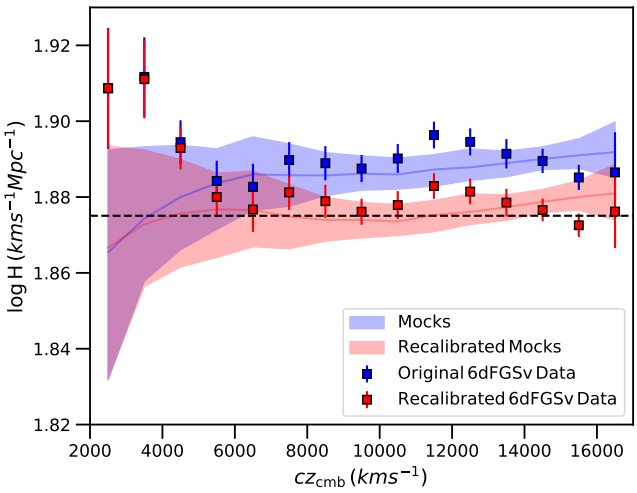

Figure 4. Measurements of the weighted mean Hubble parameter in redshift bins of width 1000 km s^{-1} from the 6dFGSv data (points) and simulations (band). The bands show the median value and 68% precentile region for the 128 mock realisations while the horizontal dashed line denotes the input value $H_0 = 75$ km s^{-1} Mpc^{-1} used to compute the distance. We expect the Hubble parameter to be roughly constant with redshift and lie close to the input value. The blue band/points show the Hubble parameter using the original 6dFGSv methodology with a magnitude limit of $J < 13.65$ for the Malmquist bias correction. The red band/points show the recalibrated results using $J < 13.38$, which clearly reduces the bias seen in the mocks. Though high, the 6dFGSv data for $cz_{\rm cmb} < 5000$ km s^{-1} are still within the 95% region computed from the simulations.

We believe this re-calibration to be robust and so use the updated 6dFGSv data in *Cosmicflows-4*. The source of the discrepancy between the magnitude limit used to construct the simulations and the optimal value found for the Malmquist bias correction is unclear, but indicates a discrepancy between the best-fit 6dFGSv Fundamental Plane (from which the simulation apparent magnitudes are derived) and the assumed magnitude limit of the data. It is not inconceivable that the true magnitude limit of the 6dFGSv data is in reality brighter than the nominal selection function, particularly in light of the other aspects of the sample selection required to go from the 2MASS photometry and 6dFGS spectra to the Fundamental Plane sample, and then again to the peculiar velocity sample. However, there may be more to the picture. A preferable solution would be to perform a joint fit for the Fundamental Plane parameters

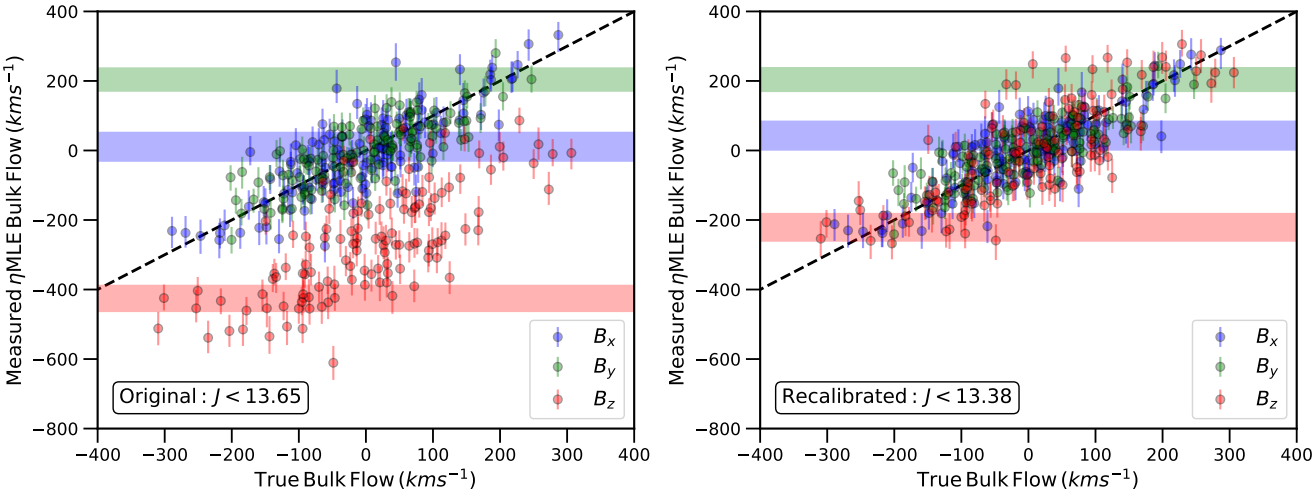

Figure 5. Measurements of the bulk flow in each direction from 6dFGSv mocks (points) and data (bands) using the ηMLE method of Qin et al. (2018). For each simulation we plot the measured maximum likelihood bulk flow against the true bulk flow calculated by averaging over the true peculiar velocity of each galaxy. The true bulk flow for the data is not known *a priori* and so the measurement is included as a horizontal band. In both cases error bars/regions denote the equal likelihood bounds encapsulating 68% of the posterior. The left hand panel shows the results using the original 6dFGSv methodology and $J < 13.65$ magnitude limit for the Malmquist bias correction/PDF normalisation. The right hand panel shows the recalibrated results using $J < 13.38$. The recalibration removes the strong negative bias in the bulk flow in the direction of the south celestial pole (z-axis in this coordinate system) seen in the simulations and believed to also be present in the data.

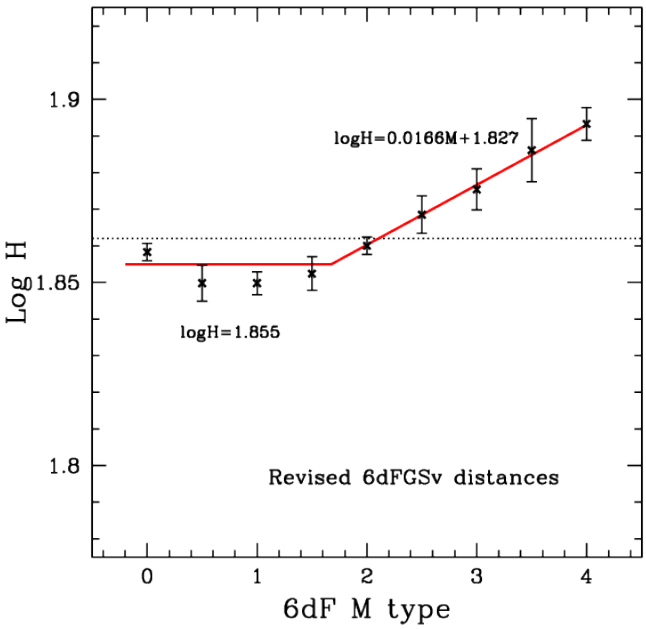

Figure 6. Trend in values of $\log H_i = \log(V_i/d_i)$ with morphological M type. Galaxies with M> 2 increasingly manifest the properties of disk systems.

and peculiar velocities simultaneously, again validated against simulations, however such an analysis is beyond the scope of the current work.

The systematic problem as a function of morphological type identified by Tully et al. (2016) remains in the revised bias adjusted 6dFGSv distances. Candidates in the 6dFGSv compilation are given a morphology M description, with M=0 for ellipticals, M=2 for lenticulars, and M=4 for spirals. As seen in Figure 6, there is a clear drift in $\langle V_i/d_i \rangle$ with M, where V_i and d_i are individual galaxy velocities and distances. The drift is in the sense that d_i values are increasingly measured too low with increasing M.

This situation is not too surprising given that the Fundamental Plane pertains to galaxy bulges. The admixture of disk contributions evidently creates a systematic. The revisions discussed above to 6dFGSv distances has not addressed this morphology-related problem. Adjustments are made to distances that statistically counter the trend seen in Fig. 6. Only the fitting parameters are changed from the adjustments made in Tully et al. (2016). The distance moduli accepted into *Cosmicflows-4* incorporate both the revised bias corrections and the morphological corrections described in this section.

4.2. *FP with SDSS Photometry and Spectroscopy*

4.3. *Combining all Fundamental Plane distances*

Just as multiple acquisitions of a distance to a spiral galaxy with photometry and rotation curve information are highly correlated, so it is the case with multiple applications of the Fundamental Plane to early type galaxies. Consequently, as an initial step we bind all the Fundamental Plane sub-samples into a joint sample. The same methodology as discussed in §3.2 is adopted to

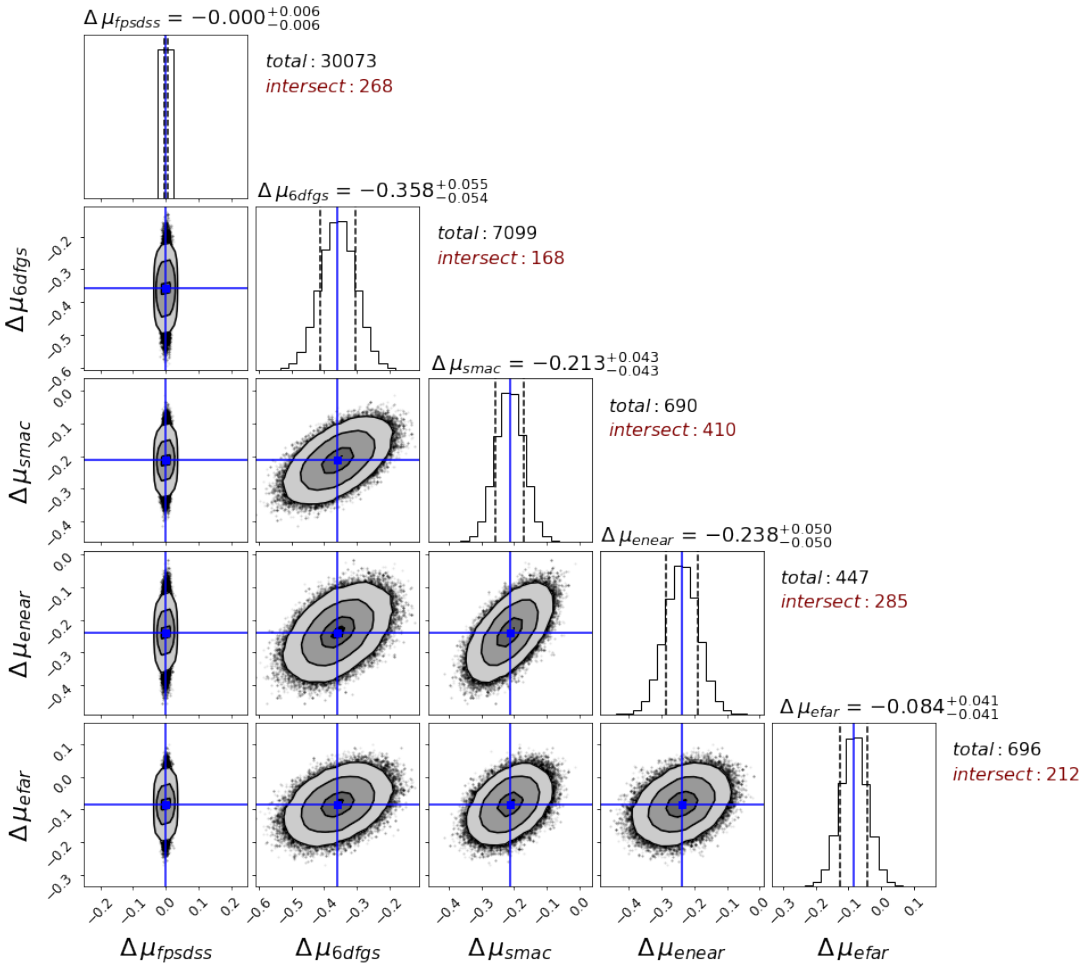

Figure 7. The posterior distribution of the optimized zero points of FP catalogs with respect to "6dFGSv". Each panel covers ±0.25 mag about the center of distribution. Other details are as in Figure 3.

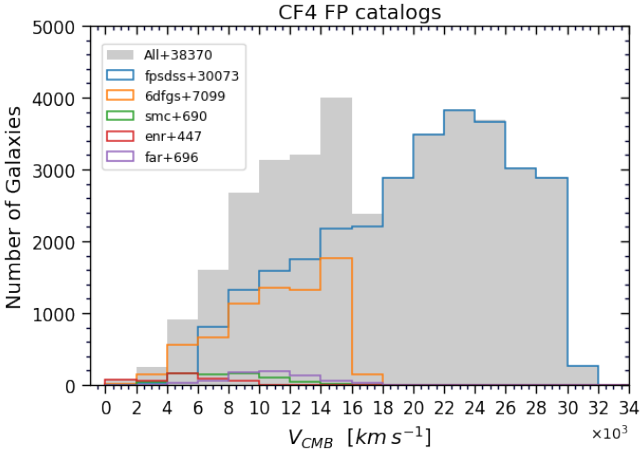

Figure 8. Cumulative histogram of FP targets with systemic velocity and a breakdown by sub-sample as given by the legend.

combine the distances of the FP catalogs of this study: "6dFGSv", "smac", "enear" and "efar". The 3.5σ rejection criterion is used to identify two outliers in "enear", one in "smac" and 17 in "6dFGSv" sub-samples. These cases are removed prior to the subsequent calculations. The "6dFGSv" distances are taken as the reference of comparisons, whence $\Delta\mu_{6dFGSv} = 0$ by our convention. Within each sub-sample, we average the distances of galaxies that reside in groups to reduce the effect of measurement uncertainties. The posterior distribution of the offset parameters ($\Delta\mu_s$) are explored with our MCMC procedure in a similar fashion to that explained in §3.2. Figure 7 illustrates the posterior distributions of the moduli offsets of "smac", "enear" and "efar" sub-samples from "6dFGSv".

5. SURFACE BRIGHTNESS FLUCTUATION DISTANCES TO EARLY TYPE GALAXIES

In predominantly ancient stellar systems, the brightest stars lie on the red giant branch where stellar envelopes inflate and hydrogen burning occurs in shells around inert helium cores. The very brightest of these

stars, at the "tip" of the red giant branch, are precursors to the onset of core helium burning and a restructuring of the star onto the horizontal branch. The passband dependence of the luminosity of a star at the tip varies with metallicity, with enhanced molecular line blanketing pushing emission redward. At solar or supersolar metallicities, the stars at the tip of the red giant branch peak in luminosity around 2 μm. The robustly-characterized luminosity of the onset of core helium burning, and the fact that it is very bright, have been exploited to measure galaxy distances.

In galaxies that can be resolved into individual stars, the preferred distance measurement methodology uses the tip of the red giant branch, to be discussed in a later section. For more distant targets, the stars blend, but the surface brightness appears mottled because of the Poisson statistics in the number of stars per resolution element, creating surface brightness fluctuations (SBF) (Tonry & Schneider 1988). The signal from the stellar fluctuations in the spatial Fourier power spectrum diminishes with distance as $1/d^2$, making it possible to measure galaxy distances with high accuracy with simple single-epoch imaging, which distinguishes SBF from other distance measurement techniques that rely on temporal monitoring (Cepheids and supernovae) or spectroscopic observations (e.g., FP and TFR).

5.1. *Sources of SBF Measurements*

We have gathered SBF distances for 508 galaxies based on five sources of SBF measurements. Two of these sources already found a presence in the earlier *Cosmicflows* compilations. Tonry et al. (2001) pioneered the methodology with observations from the ground at the optical I-band. That program targeted 300 E/S0 galaxies including essentially all E galaxies within 2,000 km s^{-1} and a sampling out to 4,000 km s^{-1}. The other earlier source of SBF distances was the HST study of E/S0 galaxies in the Virgo and Fornax clusters (Mei et al. 2007; Blakeslee et al. 2009, 2010). The exceptional spatial resolution of HST resulted in distance measurements with sufficient accuracy to resolve the three-dimensional structure of the Virgo Cluster, distinguishing the M, W, and W$'$ background galaxy groups, and to provide an accurate differential distance between the Virgo and Fornax clusters.

To the Cosmicflows-4 database we add SBF distance information from three new sources. The first of these (Cantiello et al. 2018a) is an extension of the HST Virgo Cluster study derived from the $u^\star, g, i, z$ imaging Next Generation Virgo Cluster Survey carried out with the Canada-France-Hawaii Telescope (Ferrarese et al. 2012). Our knowledge of the Virgo Cluster environs and, particularly, of the separation of the W$'$ group 50% farther away in projection and the W and M structures twice as far away, are given improved clarity with this enhanced distance database.

The second new SBF source, infrared SBF with the HST WFC3/IR camera, is a harbinger of a particularly promising improvement to the SBF methodology (Jensen et al. 2021). The wide field of view and improved sensitivity of WFC3/IR over earlier ground-based and NICMOS IR observations make it the optimal instrument for SBF measurements. Red giant stars are particularly bright in the near-IR, making IR SBF much brighter and easier to measure than at optical wavelengths, especially from space where the sky background is much less bright. Jensen et al. (2015) established the calibration for SBF in the F110W and F160W filters using observations of 16 Virgo and Fornax galaxies. As discussed in Blakeslee et al. (2021), these IR SBF distances are tied to the I-band SBF observations (Blakeslee et al. 2009), the Cepheid distance to Virgo and Fornax, and the LMC distance of 18.477 (Pietrzyński et al. 2019).

The HST F110W SBF observations reach a distance of 80 Mpc in a single orbit, for which the observational error is 4–5% (Blakeslee et al. 2021; Jensen et al. 2021). A number of different WFC3/IR F110W programs have now been mined for usable observations. Two of these programs targeted galaxies specifically for SBF distance measurements: MASSIVE seeks to understand the stellar dynamical properties and central black hole masses of massive galaxies within $\sim$ 100 Mpc (Ma et al. 2014). This study includes 41 high-quality IR SBF distances. Another targeted SBF study measured distances to 19 early-type type-Ia supernova host galaxies (Milne et al. 2020; Garnavich et al. 2020, in prep). These data sets, along with independent observations of NGC 4874 in Coma (Cho et al. 2016; Bartier et al. 2017) and NGC 4993, the 2017 gravitational wave event host (Cantiello et al. 2018b), round out a total of 62 galaxies out to 100 Mpc for which high-precision distances are now known.

The third new SBF source is minor: ground based observations of E/S0 galaxies in the Centaurus and Hydra clusters (Mieske et al. 2005). This gives precision to the relative distances of these important clusters. An interesting aspect of the Centaurus Cluster is a clear velocity bi-modality, perhaps indicative of a spatial splitting.

Figure 9 is a histogram of the cumulative SBF sample dependence on systemic velocity, with a breakdown by source.

5.2. *Combining SBF sub-samples*

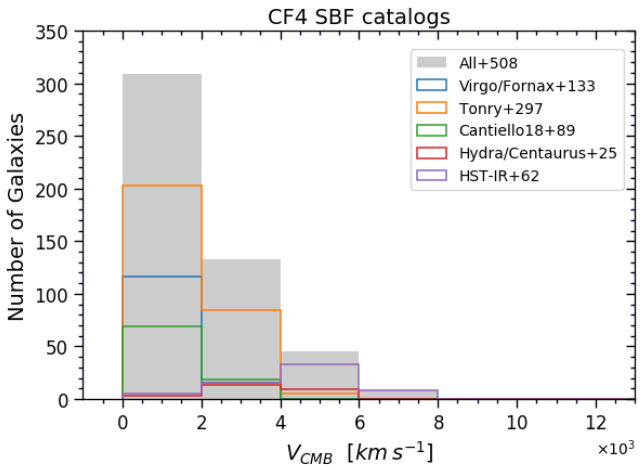

Figure 9. Cumulative histogram of SBF targets with systemic velocity and a breakdown by sub-sample as given by the legend.

There is significant overlap between only three of the five SBF sub-samples. The new IR SBF contribution overlaps with only 8 targets with Tonry. There is no overlap between the Mieske et al. Centaurus/Hydra targets and the others.

The corner plot for the three SBF sub-samples that can be compared is seen in Figure 10. The Virgo/Fornax collection based on HST optical band observations is taken as the reference. Whereas with the TF and FP studies galaxy-group comparisons help reduce errors, in the case of SBF the galaxies are relatively nearby and the individual accuracies are greater so comparisons are strictly galaxy-galaxy. The integration of the full five SBF contributions awaits the global MCMC compilation of all methodologies.

6. DISTANCES TO THE GALAXY HOSTS OF TYPE IA SUPERNOVAE

Supernovae of Type Ia (SNIa) arise in binary systems where at least one of the stars is a white dwarf. The path, or possibly paths, resulting in explosions is not resolved, with the two most discussed alternatives being, alternatively, single-degenerate models where matter from a companion accretes onto a white dwarf, or double degenerate models where two white dwarfs merge (Maoz et al. 2014). In spite of this uncertainty in the physical mechanism, the minimal dispersion in the absolute luminosities of Type Ia supernovae after a calibration based on post-maximum decline rate (Phillips 1993) can be exploited to measure galaxy distances with high accuracy. The events are sufficiently bright that SNIa at $z < 0.1$ can be discovered and monitored with moderate sized telescopes. This methodology can provide distances with 2 to 3 times the accuracy as TF and FP with considerably greater reach. Supernovae are serendipitous events, though, and the numbers of well studied occurrences remains small.

Modest samples of SNIa were included in earlier releases: 308 cases in *Cosmicflows-2*, increased to 389 in *Cosmicflows-3*. Here, those samples are augmented by contributions from four new sources, more than doubling the available sample to 933 SNIa events within $z = 0.1$. Core collapse supernovae (SNII) are proving to be useful distance tools also, although not with the same accuracy. A limited sample of SNII will be discussed in §6.1.

The new samples beyond those of *Cosmicflows-3* include 235 hosts from the Lick Observatory Supernova Search (Ganeshalingam et al. 2013), 137 hosts from the first release of the Carnegie Supernova Project (Burns et al. 2018), 669 hosts from the collection by Stahl et al. (2021), and 597 hosts in the PantheonPlus compilation (Scolnic et al. 2021?). There are considerable overlaps between these and the earlier contributions, as is evident if the contributions are summed. Diverse light curve fitters are involved. The various samples are merged in a manner analogous to that discussed in §3.2.

6.1. *Core collapse Type II supernovae*

Although SNII vary intrinsically by more than two magnitudes, the underlying events are better understood than is the case with SNIa and their luminosities correlate with observable properties. More luminous SNII have higher photospheric expansion velocities. Colors are a monitor of extinction. In *Cosmicflows-4* we include a sample of 96 SNII in 94 hosts studied by de Jaeger et al. (2020b,a). The 1σ scatter about the Hubble diagram is $\sim 15\%$ in distance, about a factor two worse than realized with SNIa.

7. TIP OF THE RED GIANT BRANCH

The Tip of the Red Giant Branch (TRGB) method for acquiring distances has two particularly resonant impacts on our program. Accuracies are typically at the level of 5% with Hubble Space Telescope observations. On the one hand, the numerous measurements now available with overlaps with other methodologies play an important role in setting the absolute scale for extragalactic distances (Freedman et al. 2019). On the other hand, the dense coverage of sources locally affords unprecedented information on a multitude of research interests. The current edition of *Cosmicflows* provides TRGB distances to 491 galaxies (Anand et al. 2021).

TRGB and the SBF procedure discussed in §5 have closely related physical bases. With SBF, the brightest stars on the red giant branch are unresolved and dis-

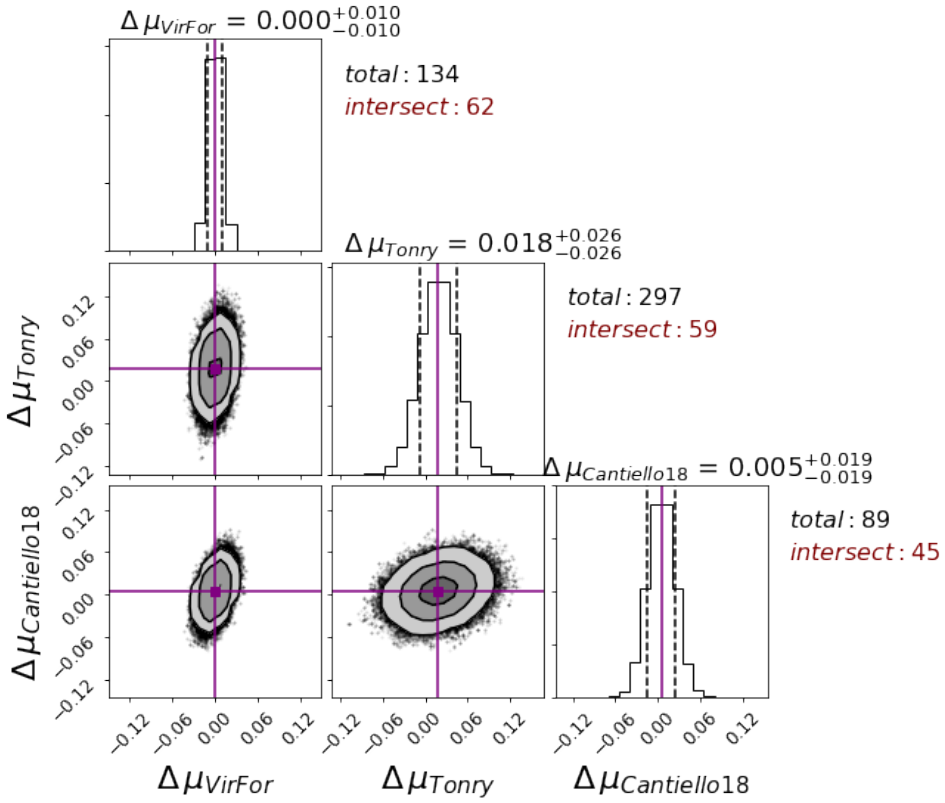

Figure 10. The posterior distribution of the optimized zero points of SBF catalogs with respect to the "Virgo-Fornax" catalog. Each panel covers ±0.15 mag about the center of distribution. Other details are as in Figure 3.

tances are inferred from the statistical properties of image mottling. With TRGB the individual brightest red giant stars can be isolated and their brightness measured. There is extensive experience with use of the TRGB as a distance tool (Da Costa & Armandroff 1990; Lee et al. 1993; Madore & Freedman 1995; Méndez et al. 2002; Makarov et al. 2006; Rizzi et al. 2007; Wu et al. 2014; McQuinn et al. 2017; Jang & Lee 2017; Beaton et al. 2018).

In practise, SBF and TRGB are most effective in two distinct regimes. There are concerns with contamination from young populations and metallicity effects that are addressed in different ways. In the case of SBF, the most stable candles are very old and high metallicity systems, with relative intrinsic magnitude constancy in the infrared. In the case of TRGB, the optimal target stars have low metallicity and are observed near to 900 μm where metallicity and age effects are minimal. Such stars are best sought in the halos of galaxies where there is minimal extinction or crowding or contamination from young populations.

While several groups have been involved with TRGB studies, with a partial literature given above, all results reported in *Cosmicflows* have been drawn from data in the HST archives and analyzed in a uniform way with our standard procedures (Jacobs et al. 2009; Anand et al. 2021). Proceeding from *Cosmicflows-2* to −3 to −4, our collection of TRGB distances has grown from 297 to 384 to 491. Ninety percent of galaxies brighter than $M_B = -13$ within 10 Mpc now have distance estimates with 5% accuracy. This material has given rise to population studies of individual systems (Makarova et al. 2017; Karachentsev et al. 2017), to studies of the grouping properties of galaxies (Kourkchi & Tully 2017), and to studies of local filamentary structure and motions (Shaya et al. 2017; Anand et al. 2019).

The histogram of TRGB candidates with systemic velocity is seen in Figure ?? and the distribution on the sky is seen in Figure ???. Given that most of the TRGB systems are within 10 Mpc because of the single orbit capabilities of HST, these candidates are mostly to be found in the restricted sector of the sky of our home Local Sheet (Tully et al. 2008).

The present zero point of our TRGB distances was established with the study by Rizzi et al. (2007). This calibration follows from the identification of the Horizontal Branch in five Local Group galaxies (Sculptor, Fornax, and NGC 185 spheroidals, the irregular IC 1613, and the spiral M33) assuming the Horizontal Branch absolute magnitude found by Carretta et al. (2000) and the

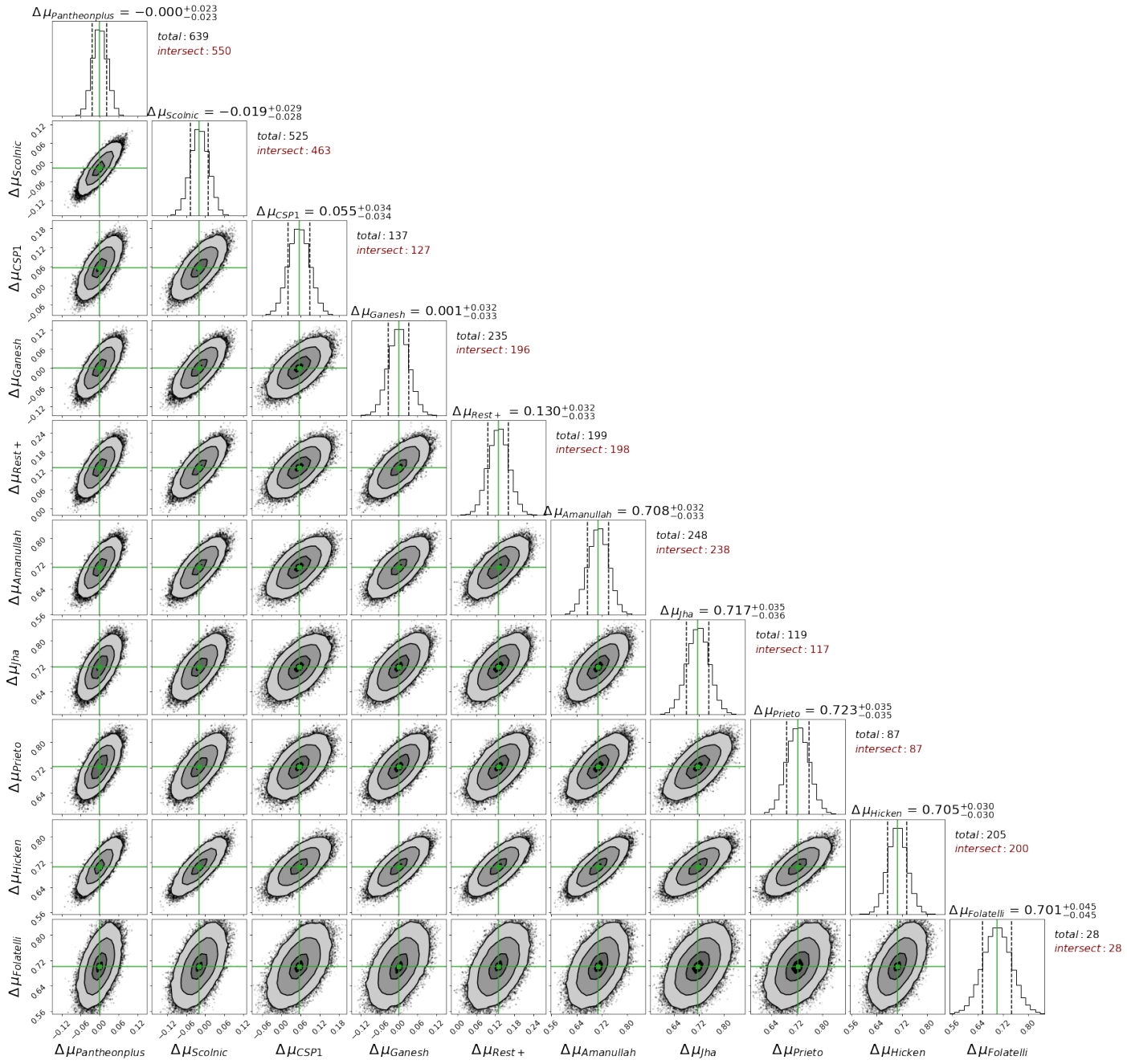

Figure 11. The posterior distribution of the optimized zero points of SNIa catalogs with respect to the Pantheonplus distance moduli. Each panel covers ±0.15 mag about the center of distribution. Other details are as in Figure 3.

implications for the absolute magnitude of the TRGB drawn from those systems. As a check, consistency was found between the TRGB and maser distances of NGC 4258. There have been more recent calibrations of the TRGB zero point and there has been some dispute (Jang & Lee 2017; McQuinn et al. 2017; Freedman et al. 2019; Yuan et al. 2019; Freedman et al. 2020). We have revisited the comparison between the maser distance to NGC 4258 with the updated value of $d_{maser} = 7.568 \pm 0.082$ (stat) ± 0.076 (sys) Mpc (Reid et al. 2019) with $d_{trgb} = 7.748 \pm ?$ from new HST observations (Anand et al. 2021c). The TRGB absolute scale at this stage is provisional. The calibration will be reviewed in §10. In any event, a post-Gaia analysis of the TRGB scale in the spirit of the Rizzi et al. (2007) study is warranted.

8. CEPHEID PERIOD LUMINOSITY RELATION

The Cepheid Period Luminosity Relation (CPLR) or Leavitt Law (Leavitt & Pickering 1912) has been con-

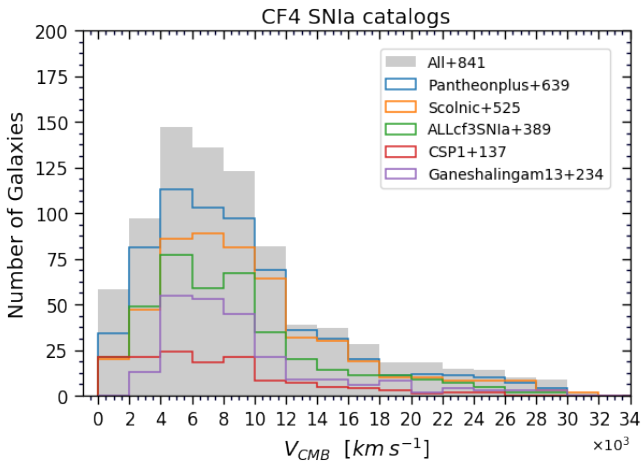

Figure 12. Cumulative histogram of SNIa targets with systemic velocity and a breakdown by sub-sample as given by the legend.

sidered the gold standard as a method for measuring absolute galaxy distances. We accept a combined sample of 58 systems into *Cosmicflows-4*. Our reference compilation of 22 objects is that given by Riess et al. (2016, 2019), see also Yuan et al. (2020, 2021), assuming the Detached Eclipsing Binary distance modulus of $\mu_{LMC} = 18.477 \pm 0.004$ (stat) ± 0.026 (sys) of Pietrzyński et al. (2019) ($d_{LMC} = 49.59 \pm 0.09$ Mpc). We also use 23 non-overlapping systems observed in the course of the HST key project to measure H_0 (Freedman et al. 2001) shifted to the LMC distance given above. We include 12 systems all within $\sim$ 3 Mpc observed from ground based observatories and reported by Bhardwaj et al. (2016) and the Araucaria collaboration (Zgirski et al. 2017), with scales to our LMC distance. The final case observed with HST and on our LMC scale is for NGC 6814 (Bentz et al. 2019).

The absolute calibration of the CPLR remains a work in progress. Cepheid variables are young stars that tend to live in crowded, dusty environments. It remains to be resolved if there are metallicity dependencies. There are expectations of a more refined scaling once parallax information provided by Gaia is digested (Riess et al. 2021). Our final scaling with *Cosmicflows-4* will be reviewed in §10.

9. NUCLEAR MASERS

The fortuitous occurrence of a water maser in the nucleus of NGC 4258 is making an out-sized contribution to studies of the extragalactic distance scale because the well defined geometry of the event (Humphreys et al. 2013; Reid et al. 2019). Observations of the positions, velocities, and accelerations of the maser signals can be modelled to give a direct geometric estimate of the angular-diameter distance of the galaxy without recourse to information external to the system. The situation in the case of NGC 4258 is particularly favorable because the plane of rotation of the masers is almost edge-on and the very long baseline radio interferometric signals are strong. The measured distance modulus is 29.397 ± 0.032, a formal error of only 1.5% in distance.

The occurrence in NGC 4258 is fortuitous indeed because extensive searches have, to date, only turned up five more cases that have warranted the attention leading to publication (Pesce et al. 2020). Uncertainties vary wildly (median $\sim$ 10%) because signals are weak and geometries are less favorable. Distances for all of these systems are included in *Cosmicflows-4* at their geometrically determined distances. While non-geometric distances are subject to modification in the Bayesian analysis to follow, the maser distances (with associated uncertainties) are fixed.

10. ALL TOGETHER

11. SUMMARY

REFERENCES

Adhikari, S., Dalal, N., & Chamberlain, R. T. 2014, JCAP, 2014, 019, doi: 10.1088/1475-7516/2014/11/019

Anand, G. S., Tully, R. B., Rizzi, L., Shaya, E. J., & Karachentsev, I. D. 2019, ApJ, 880, 52, doi: 10.3847/1538-4357/ab24e5

Anand, G. S., Rizzi, L., Tully, R. B., et al. 2021, arXiv e-prints, arXiv:2104.02649. https://arxiv.org/abs/2104.02649

Bartier, C.-L., Jensen, J., & Blakeslee, J. 2017, in American Astronomical Society Meeting Abstracts, Vol. 229, American Astronomical Society Meeting Abstracts #229, 143.05

Beaton, R. L., Bono, G., Braga, V. F., et al. 2018, SSRv, 214, 113, doi: 10.1007/s11214-018-0542-1

Benedict, G. F., McArthur, B. E., Feast, M. W., et al. 2007, AJ, 133, 1810, doi: 10.1086/511980

Bentz, M. C., Ferrarese, L., Onken, C. A., Peterson, B. M., & Valluri, M. 2019, ApJ, 885, 161, doi: 10.3847/1538-4357/ab48fb

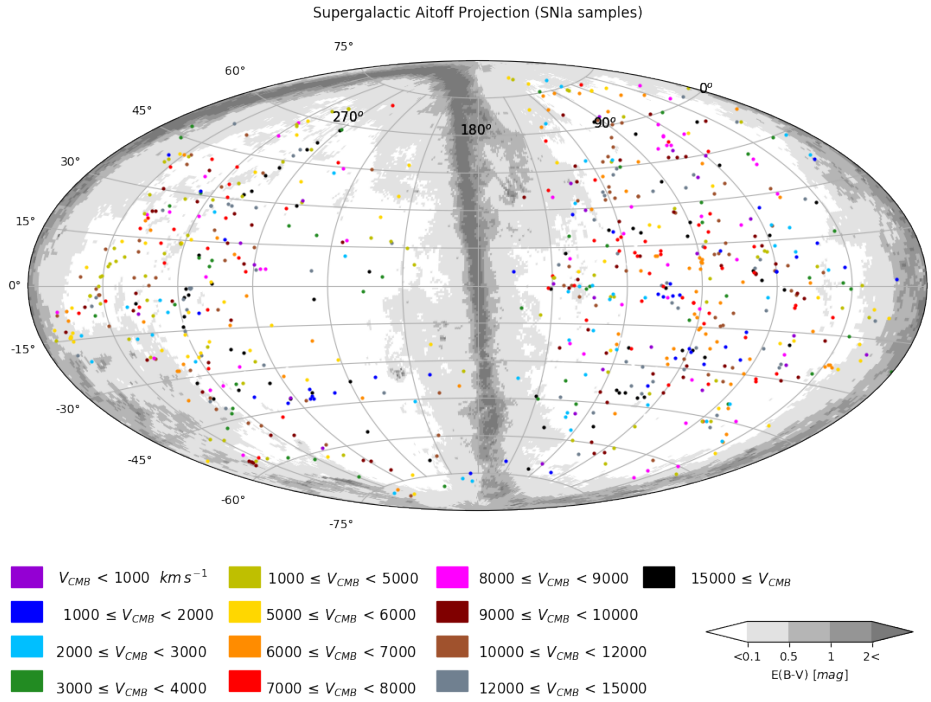

Figure 13. An aitoff projection in supergalactic coordinates of the distribution of the ensemble of SNIa samples. Colors relate to systemic velocities of the group of a galaxy as given in the table below the map. Milky Way extinction levels are cast in shades of grey.

Bernardi, M., Alonso, M. V., da Costa, L. N., et al. 2002, AJ, 123, 2990, doi: 10.1086/340463

Bhardwaj, A., Kanbur, S. M., Macri, L. M., et al. 2016, AJ, 151, 88, doi: 10.3847/0004-6256/151/4/88

Blakeslee, J. P., Jensen, J. B., Ma, C.-P., Milne, P. A., & Greene, J. E. 2021, ApJ, 911, 65, doi: 10.3847/1538-4357/abe86a

Blakeslee, J. P., Jordán, A., Mei, S., et al. 2009, ApJ, 694, 556, doi: 10.1088/0004-637X/694/1/556

Blakeslee, J. P., Cantiello, M., Mei, S., et al. 2010, ApJ, 724, 657, doi: 10.1088/0004-637X/724/1/657

Burns, C. R., Parent, E., Phillips, M. M., et al. 2018, ApJ, 869, 56, doi: 10.3847/1538-4357/aae51c

Campbell, L. A., Lucey, J. R., Colless, M., et al. 2014, MNRAS, 443, 1231, doi: 10.1093/mnras/stu1198

Cantiello, M., Blakeslee, J. P., Ferrarese, L., et al. 2018a, ApJ, 856, 126, doi: 10.3847/1538-4357/aab043

Cantiello, M., Jensen, J. B., Blakeslee, J. P., et al. 2018b, ApJL, 854, L31, doi: 10.3847/2041-8213/aaad64

Carretta, E., Gratton, R. G., Clementini, G., & Fusi Pecci, F. 2000, ApJ, 533, 215, doi: 10.1086/308629

Cho, H., Blakeslee, J. P., Chies-Santos, A. L., et al. 2016, ApJ, 822, 95, doi: 10.3847/0004-637X/822/2/95

Clementini, G., Garofalo, A., Muraveva, T., & Ripepi, V. 2018, in Astronomical Society of the Pacific Conference Series, Vol. 514, Stellar Populations and the Distance Scale, ed. J. Jensen, R. M. Rich, & R. de Grijs, 89. https://arxiv.org/abs/1804.09575

Colless, M., Saglia, R. P., Burstein, D., et al. 2001, MNRAS, 321, 277

Courtois, H. M., Tully, R. B., Fisher, J. R., et al. 2009, AJ, 138, 1938, doi: 10.1088/0004-6256/138/6/1938

Courtois, H. M., Tully, R. B., & Héraudeau, P. 2011a, MNRAS, 415, 1935, doi: 10.1111/j.1365-2966.2011.18839.x

Courtois, H. M., Tully, R. B., Makarov, D. I., et al. 2011b, MNRAS, 414, 2005, doi: 10.1111/j.1365-2966.2011.18515.x

Da Costa, G. S., & Armandroff, T. E. 1990, AJ, 100, 162, doi: 10.1086/115500

de Jaeger, T., Stahl, B. E., Zheng, W., et al. 2020a, MNRAS, 496, 3402, doi: 10.1093/mnras/staa1801

de Jaeger, T., Galbany, L., González-Gaitán, S., et al. 2020b, MNRAS, 495, 4860, doi: 10.1093/mnras/staa1402

Djorgovski, S., & Davis, M. 1987, ApJ, 313, 59, doi: 10.1086/164948

Dressler, A., Lynden-Bell, D., Burstein, D., et al. 1987, ApJ, 313, 42, doi: 10.1086/164947

Ferrarese, L., Côté, P., Cuilland re, J.-C., et al. 2012, ApJS, 200, 4, doi: 10.1088/0067-0049/200/1/4
Foreman-Mackey, D., Hogg, D. W., Lang, D., & Goodman, J. 2013, PASP, 125, 306, doi: 10.1086/670067
Freedman, W. L., Madore, B. F., Gibson, B. K., et al. 2001, ApJ, 553, 47, doi: 10.1086/320638
Freedman, W. L., Madore, B. F., Hatt, D., et al. 2019, ApJ, 882, 34, doi: 10.3847/1538-4357/ab2f73
Freedman, W. L., Madore, B. F., Hoyt, T., et al. 2020, ApJ, 891, 57, doi: 10.3847/1538-4357/ab7339
Ganeshalingam, M., Li, W., & Filippenko, A. V. 2013, MNRAS, 433, 2240, doi: 10.1093/mnras/stt893
Haynes, M. P., Giovanelli, R., Martin, A. M., et al. 2011, AJ, 142, 170, doi: 10.1088/0004-6256/142/5/170
Haynes, M. P., Giovanelli, R., Kent, B. R., et al. 2018, ApJ, 861, 49, doi: 10.3847/1538-4357/aac956
Hong, T., Staveley-Smith, L., Masters, K. L., et al. 2019, MNRAS, 487, 2061, doi: 10.1093/mnras/stz1413
Huchra, J. P., Macri, L. M., Masters, K. L., et al. 2012, ApJS, 199, 26, doi: 10.1088/0067-0049/199/2/26
Hudson, M. J., Lucey, J. R., Smith, R. J., Schlegel, D. J., & Davies, R. L. 2001, MNRAS, 327, 265, doi: 10.1046/j.1365-8711.2001.04786.x
Humphreys, E. M. L., Reid, M. J., Moran, J. M., Greenhill, L. J., & Argon, A. L. 2013, ApJ, 775, 13, doi: 10.1088/0004-637X/775/1/13
Jacobs, B. A., Rizzi, L., Tully, R. B., et al. 2009, AJ, 138, 332, doi: 10.1088/0004-6256/138/2/332
Jang, I. S., & Lee, M. G. 2017, ApJ, 835, 28, doi: 10.3847/1538-4357/835/1/28
Jarrett, T. H., Chester, T., Cutri, R., et al. 2000, AJ, 119, 2498, doi: 10.1086/301330
Jensen, J. B., Blakeslee, J. P., Gibson, Z., et al. 2015, ApJ, 808, 91, doi: 10.1088/0004-637X/808/1/91
Jensen, J. B., Blakeslee, J. P., Ma, C.-P., et al. 2021, arXiv e-prints, arXiv:2105.08299. https://arxiv.org/abs/2105.08299
Jones, D. H., Read, M. A., Saunders, W., et al. 2009, MNRAS, 399, 683, doi: 10.1111/j.1365-2966.2009.15338.x
Kaiser, N. 1988, MNRAS, 231, 149, doi: 10.1093/mnras/231.2.149
Karachentsev, I. D., Makarova, L. N., Tully, R. B., et al. 2017, MNRAS, 469, L113, doi: 10.1093/mnrasl/slx061
Kourkchi, E., & Tully, R. B. 2017, ApJ, 843, 16, doi: 10.3847/1538-4357/aa76db
Kourkchi, E., Tully, R. B., Anand, G. S., et al. 2020a, ApJ, 896, 3, doi: 10.3847/1538-4357/ab901c
Kourkchi, E., Tully, R. B., Neill, J. D., et al. 2019, ApJ, 884, 82, doi: 10.3847/1538-4357/ab4192
Kourkchi, E., Tully, R. B., Eftekharzadeh, S., et al. 2020b, ApJ, 902, 145, doi: 10.3847/1538-4357/abb66b
Leavitt, H. S., & Pickering, E. C. 1912, Harvard College Observatory Circular, 173, 1
Lee, M. G., Freedman, W. L., & Madore, B. F. 1993, ApJ, 417, 553, doi: 10.1086/173334
Lim, S. H., Mo, H. J., Lu, Y., Wang, H., & Yang, X. 2017, MNRAS, 470, 2982, doi: 10.1093/mnras/stx1462
Ma, C.-P., Greene, J. E., McConnell, N., et al. 2014, ApJ, 795, 158, doi: 10.1088/0004-637X/795/2/158
Madore, B. F., & Freedman, W. L. 1995, AJ, 109, 1645, doi: 10.1086/117391
Magoulas, C., Springob, C. M., Colless, M., et al. 2012, MNRAS, 427, 245, doi: 10.1111/j.1365-2966.2012.21421.x
Makarov, D., Makarova, L., Rizzi, L., et al. 2006, AJ, 132, 2729, doi: 10.1086/508925
Makarov, D. I., Zaitseva, N. A., & Bizyaev, D. V. 2018, MNRAS, 479, 3373, doi: 10.1093/mnras/sty1629
Makarova, L. N., Makarov, D. I., Karachentsev, I. D., Tully, R. B., & Rizzi, L. 2017, MNRAS, 464, 2281, doi: 10.1093/mnras/stw2502
Maoz, D., Mannucci, F., & Nelemans, G. 2014, ARA&A, 52, 107, doi: 10.1146/annurev-astro-082812-141031
McQuinn, K. B. W., Skillman, E. D., Dolphin, A. E., Berg, D., & Kennicutt, R. 2017, AJ, 154, 51, doi: 10.3847/1538-3881/aa7aad
Mei, S., Blakeslee, J. P., Côté, P., et al. 2007, ApJ, 655, 144, doi: 10.1086/509598
Méndez, B., Davis, M., Moustakas, J., et al. 2002, AJ, 124, 213, doi: 10.1086/341168
Mieske, S., Hilker, M., & Infante, L. 2005, A&A, 438, 103, doi: 10.1051/0004-6361:20041583
Mould, J., Clementini, G., & Da Costa, G. 2019, PASA, 36, e001, doi: 10.1017/pasa.2018.46
Paturel, G., Garnier, R., Petit, C., & Marthinet, M. C. 1996, A&A, 311, 12
Pesce, D. W., Braatz, J. A., Reid, M. J., et al. 2020, ApJL, 891, L1, doi: 10.3847/2041-8213/ab75f0
Phillips, M. M. 1993, ApJL, 413, L105, doi: 10.1086/186970
Pietrzyński, G., Graczyk, D., Gallenne, A., et al. 2019, Nature, 567, 200, doi: 10.1038/s41586-019-0999-4
Qin, F., Howlett, C., & Staveley-Smith, L. 2019, MNRAS, 487, 5235, doi: 10.1093/mnras/stz1576
Qin, F., Howlett, C., Staveley-Smith, L., & Hong, T. 2018, MNRAS, 477, 5150, doi: 10.1093/mnras/sty928
Reid, M. J., Pesce, D. W., & Riess, A. G. 2019, ApJL, 886, L27, doi: 10.3847/2041-8213/ab552d
Riess, A. G., Casertano, S., Yuan, W., et al. 2021, ApJL, 908, L6, doi: 10.3847/2041-8213/abdbaf

Riess, A. G., Casertano, S., Yuan, W., Macri, L. M., & Scolnic, D. 2019, ApJ, 876, 85, doi: 10.3847/1538-4357/ab1422

Riess, A. G., Macri, L. M., Hoffmann, S. L., et al. 2016, ApJ, 826, 56, doi: 10.3847/0004-637X/826/1/56

Rizzi, L., Tully, R. B., Makarov, D., et al. 2007, ApJ, 661, 815, doi: 10.1086/516566

Shaya, E. J., Tully, R. B., Hoffman, Y., & Pomarède, D. 2017, ApJ, 850, 207, doi: 10.3847/1538-4357/aa9525

Skrutskie, M. F., Cutri, R. M., Stiening, R., et al. 2006, AJ, 131, 1163, doi: 10.1086/498708

Sorce, J. G., Courtois, H. M., & Tully, R. B. 2012, AJ, 144, 133, doi: 10.1088/0004-6256/144/5/133

Sorce, J. G., Tully, R. B., Courtois, H. M., et al. 2014, MNRAS, 444, 527, doi: 10.1093/mnras/stu1450

Springob, C. M., Masters, K. L., Haynes, M. P., Giovanelli, R., & Marinoni, C. 2007, ApJS, 172, 599, doi: 10.1086/519527

Springob, C. M., Magoulas, C., Colless, M., et al. 2014, MNRAS, 445, 2677, doi: 10.1093/mnras/stu1743

Stahl, B. E., de Jaeger, T., Boruah, S. S., et al. 2021, MNRAS, doi: 10.1093/mnras/stab1446

Tempel, E., Tamm, A., Gramann, M., et al. 2014, A&A, 566, A1, doi: 10.1051/0004-6361/201423585

Tonry, J., & Schneider, D. P. 1988, AJ, 96, 807, doi: 10.1086/114847

Tonry, J. L., Dressler, A., Blakeslee, J. P., et al. 2001, ApJ, 546, 681, doi: 10.1086/318301

Tully, R. B. 2015a, AJ, 149, 54, doi: 10.1088/0004-6256/149/2/54

—. 2015b, AJ, 149, 171, doi: 10.1088/0004-6256/149/5/171

Tully, R. B., Courtois, H. M., & Sorce, J. G. 2016, AJ, 152, 50, doi: 10.3847/0004-6256/152/2/50

Tully, R. B., & Fisher, J. R. 1977, A&A, 54, 661

Tully, R. B., Shaya, E. J., Karachentsev, I. D., et al. 2008, ApJ, 676, 184, doi: 10.1086/527428

Tully, R. B., Courtois, H. M., Dolphin, A. E., et al. 2013, AJ, 146, 86, doi: 10.1088/0004-6256/146/4/86

Wright, E. L., Eisenhardt, P. R. M., Mainzer, A. K., et al. 2010, AJ, 140, 1868, doi: 10.1088/0004-6256/140/6/1868

Wu, P.-F., Tully, R. B., Rizzi, L., et al. 2014, AJ, 148, 7, doi: 10.1088/0004-6256/148/1/7

York, D. G., Adelman, J., Anderson, John E., J., et al. 2000, AJ, 120, 1579, doi: 10.1086/301513

Yuan, W., Riess, A. G., Macri, L. M., Casertano, S., & Scolnic, D. M. 2019, ApJ, 886, 61, doi: 10.3847/1538-4357/ab4bc9

Yuan, W., Fausnaugh, M. M., Hoffmann, S. L., et al. 2020, ApJ, 902, 26, doi: 10.3847/1538-4357/abb377

Yuan, W., Macri, L. M., Peterson, B. M., et al. 2021, ApJ, 913, 3, doi: 10.3847/1538-4357/abf24a

Zgirski, B., Gieren, W., Pietrzyński, G., et al. 2017, ApJ, 847, 88, doi: 10.3847/1538-4357/aa88c4